Nano Research
2021, 14(12): 4833–4840
ISSN 1998-0124 CN 11-5974/O4
https://doi.org/10.1007/s12274-021-3437-5

Research Article

MXene based mechanically and electrically enhanced film for triboelectric nanogenerator

Yuyu Gao[1,2,§], Guoxu Liu[1,3,§], Tianzhao Bu[1,3], Yaoyao Liu[1,3], Youchao Qi[1,3], Yanting Xie[2], Shaohang Xu[1,3], Weili Deng[2], Weiqing Yang[2] (✉), and Chi Zhang[1,3,4] (✉)

[1] *CAS Center for Excellence in Nanoscience, Beijing Key Laboratory of Micro-nano Energy and Sensor, Beijing Institute of Nanoenergy and Nanosystems Chinese Academy of Sciences, Beijing 101400, China*
[2] *Key Laboratory of Advanced Technologies of Materials (Ministry of Education), School of Materials Science and Engineering, Southwest Jiaotong University, Chengdu 610031, China*
[3] *School of Nanoscience and Technology, University of Chinese Academy of Sciences, Beijing 100049, China*
[4] *Center on Nanoenergy Research, School of Physical Science and Technology, Guangxi University, Nanning 530004, China*
[§] *Yuyu Gao and Guoxu Liu contributed equally to this work.*

Received: 30 December 2020 / **Revised:** 23 February 2021 / **Accepted:** 3 March 2021

ABSTRACT

The development of triboelectric nanogenerator (TENG) technology which can directly convert ambient mechanical energy into electric energy may affect areas from green energy harvesting to emerging wearing electronics. And, the material of triboelectric layer is critical to the mechanical robustness and electrical output characteristics of the TENGs. Herein, a MXene enhanced electret polytetrafluoroethylene (PTFE) film with a high mechanical property and surface charge density is developed. The MXene/PTFE composite film was synthesized by spraying and annealing treatment. With the doping of MXene, the crystallinity of composite film could be tuned, leading to an enhancement in the tensile property of 450% and reducing the wear volume about 80% in the friction test. Furthermore, the as-fabricated TENG with this composite film outputs 397 V of open-circuit voltage, 21 μA of short-circuit current, and 232 nC of transfer charge quantity, which are 4, 6, and 6 times higher than that of the TENG made by pure PTFE film, respectively. Therefore, this work provides a creative strategy to simultaneously improve the mechanical property and electrical performance of the TENGs, which have great potential in improving device stability under a complex mechanical environment.

KEYWORDS

MXene, polytetrafluoroethylene (PTFE), mechanically and electrically enhanced, triboelectric layer, triboelectric nanogenerator

1 Introduction

On the demand of healthcare or environment monitoring, distributed equipment including wearable electronics [1–3], internet of thing (IoT) devices [4–6], smart facilities [7, 8], play an increasingly important role in our daily life. However, one critical challenge identified in this field is how to power up these devices sustainably [9–13]. Thus, collecting energy from renewable sources [14–19] like wind, ocean wave, solar and thermal is gradually attracting the attention of researchers. In the past several years, comparing with the traditional electromagnetic generator, triboelectric nanogenerator (TENG), which is based on the second term of Maxwell's displacement current [20–22], has been demonstrated its great advantages in the low-frequency, light-weight and low-cost [15, 23, 24]. As the reason, the TENG has been extensively researched in energy harvesting devices and self-powered sensors [25–27]. However, to make it more practical in actual application, researchers are keeping pursuing various methods for improving the performance of the TENG [28–32].

Typically, the TENG consists of two kinds of materials with different electronegativity and corresponding electrodes [33]. In the contact-separation mode, two triboelectric layers contact and separate from each other, leading to the electron transfer between the surfaces of two triboelectric layers and causing the reciprocating induction current in the external circuit [34–39]. Therefore, the study on triboelectric layer material is one of the key factors to improve the performance of TENG. Series of materials, which commonly appeared in our daily life, have been studied seriously to investigate the ability of electrostatic induction. Among them, polytetrafluoroethylene (PTFE), one of the materials at the end of the triboelectric series [40], has been vastly applied in TENG devices. Moreover, various methods were developed to further enhance the TENG's output performance. For instance, the surface modification [41, 42] can improve the surface roughness via creating a micro/nanostructure or introduce some electronegative function group [43] on the material surfaces to change the electron affinity of the triboelectric layer. Another way is manipulating the charge storage ability [44–46] of the triboelectric layer by doping some conductive particles like Au nanoparticles [47] and active carbon particles [48]. Nevertheless, most of the previous works are focusing on promoting electrical output performance, few of them consider the mechanical property enhancement, which

Address correspondence to Chi Zhang, czhang@binn.cas.cn; Weiqing Yang, wqyang@swjtu.edu.cn

is also quite important to the robustness of the TENG.

MXene [49], as a new kind of two-dimensional material, owing to its excellent conductivity, high specific area, and good mechanical strength, has been used in many fields [50–54]. It has been demonstrated that MXene has the triboelectric ability [55], similar to PTFE, which is attributed to the electric negative functional group like –OH, –F. Herein, we introduce an MXene enhanced PTFE composite film achieving high mechanical strength and high relative electronegativity. Different amounts of the MXene flakes were doped into the PTFE aqueous emulsion and the composite film was obtained via spray coating method. After annealing treatment, the crystallinity of PTFE could be tuned, which can greatly affect the mechanical property of the composite film. Besides, with the synergistic effect of the MXene, the obtained composite film shows a great enhancement in tensile property up to 450% and wear volume is reduced more than 80% in the friction test. Due to the addition of the conductive MXene material, the composite film exhibits a greater electric charge storage ability and the fabricated TENG shows a 397 V of open-circuit voltage, 21 μA of short-circuit current, and 232 nC of transfer charge quantity, which are 4, 6 and 6 times higher than that of TENG made by PTFE film without MXene doping. And the charge speed for a 1 μF capacitor is almost 37 times faster. Hence, this work reported a new strategy that can simultaneously improve the mechanical property and the electrical performance of the TENG, which has great potential to improve the stability of the TENG.

2 Experimental

2.1 Preparation of MXene

MXene was obtained by etching the commercial MAX (Ti_3AlC_2 11 Technology Co., Ltd., China) by using HF (49 wt.%, MACKLIM Co., Ltd., China). 2 g MAX was added into 20 mL HF solution and stirring by a magnetic stirring table at 40 °C for 24 h to remove the aluminium element. After that, the obtained solution was centrifuged and washed by deionized water many times until the pH of the solution is about 6–7. Subsequently, the sediment dispersed in deionized water and ultrasonicate for 1 h to acquire the blackish green supernatant.

2.2 Preparation of composite film and fabrication of the TENG

Different amounts of MXene from 0 to 35 mg were added into 2 mL pure PTFE aqueous emulsion (DISP 40, Dupont, American) and stirred for 5 min at 1,000 rpm. And then the commercial spray gun (W-101, Qi Yan, Japanese) was used to spray on Cu substrate and then put it into chemical vapor deposition (CVD). Argon gas as the protective gas will be turned on for 30 min before and during the whole annealing process at the rate of 100 ccm. Next, CVD begins to heat up from room temperature to 380 °C at the rate of 3 °C/min, then the temperature was kept for 30 min, subsequently cool down to room temperature for about 7–8 h. Finally, the composite film could be obtained. The obtained composite would be polarized at 6 kV for 3 min and fixed on a linear-motor ready for the contact-separation test with another Cu plate.

2.3 Material characteristic

Surface morphology images of the MXene and composite film were carried by the ultra-high resolution field emission scanning electron microscope (SEM, SU 8020, Hitachi, Japanese) with an accelerating voltage of 10 kV. Raman spectra were acquired by Labram Hr Evolution (HORIBA, France). Attenuated total reflectance Fourier transform infrared (ATR-FTIR) spectra were acquired by VERTEX 80v (Bruker, German). Differential scanning calorimeter (DSC) spectra were acquired by Q2000 (TA, USA). X-ray diffraction (XRD) spectra were acquired by X Pert Pro (Holland) X-ray diffract meter with Cu Kα1 radiation (λ = 0.154 nm) from 5° to 90°.

2.4 TENG performance measurement

Electrical performance was measured by a low-noise electrometer (Keithley 6514, USA). Tensile test was carried on a universal

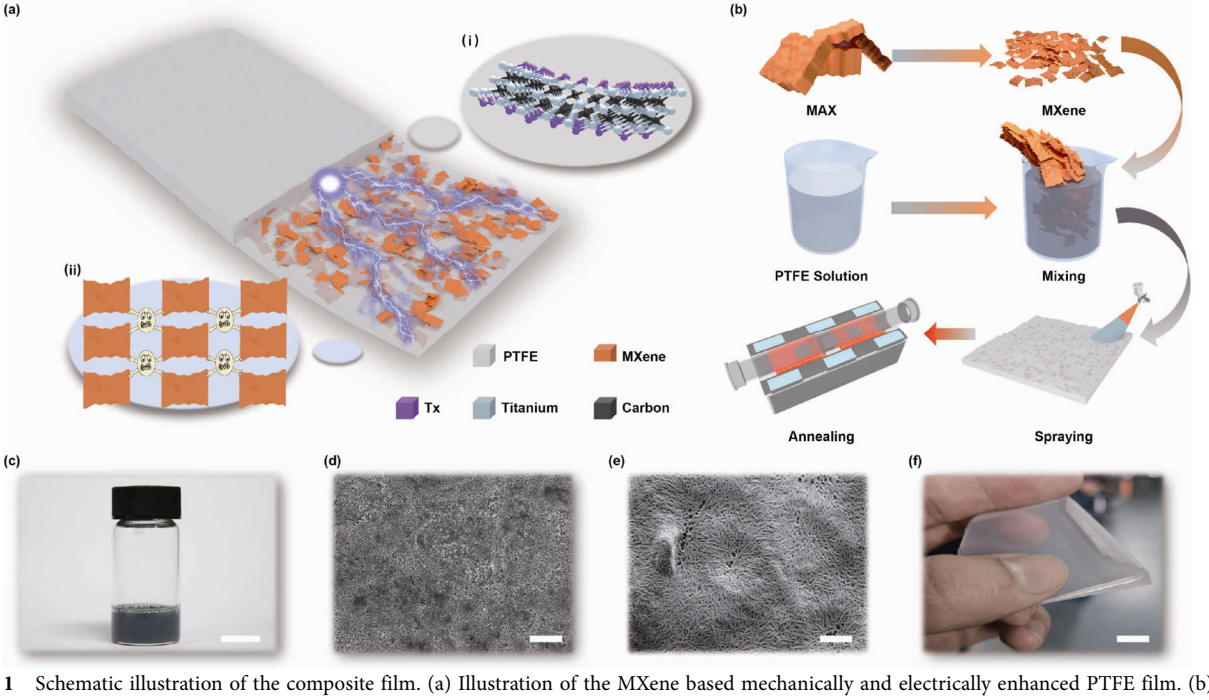

Figure 1 Schematic illustration of the composite film. (a) Illustration of the MXene based mechanically and electrically enhanced PTFE film. (b) The fabrication process of the composite film. (c) Photograph of the PTFE/MXene aqueous emulsion (10 mg MXene). Scale bar: 1.5 cm. (d) SEM image of the sprayed PTFE/MXene film before heat treatment. Scale bar: 2.5 μm. (e) SEM image of the sprayed PTFE/MXene film after heat treatment. Scale bar: 10 μm. (f) Photograph of the obtained film. Scale bar: 1 cm.

testing machine (Mark 10, USA) at the speed of 10 mm/min. Friction test was carried by a UMT-Tribo Lab (Bruker, German) under 1 Hz with a steel grinding ball with the diameter of 6 mm.

3 Result and discussions

Figure 1(a) schematically presents the structure of the composite film. Figure 1(a)(i) is the molecular structure of MXene ($Ti_3C_2T_x$) and Fig. 1(a)(ii) shows the interconnection between MXene flakes and PTFE. The composite film is made of PTFE and MXene flakes, and the MXene flakes were distributed evenly among the film. The fabrication procedures are shown in Fig. 1(b). MXene flakes were obtained by using the traditional method to etch the "A" layer from its parent phase-MAX. Then, MXene aqueous solution with specific concentrations (the corresponding doping amount of MXene is 0–35 mg) were added into PTFE aqueous emulsion. With a thoroughly stirring process, MXene flakes uniformly dispersed in the mixed solution, and the color of the mixture turned from white to gray as shown in Fig. 1(c). Next, by using the commercial spray gun, the MXene/PTFE mixture was directly sprayed on the copper plate to form the MXene/PTFE composite film, in which the copper plate plays the role of both substrate and electrode, before annealing process. The surface detail of the composite film was shown in Fig. 1(d). It is obvious that numerous PTFE nano sphere-particles with average size of about 200 nm densely dispersed on the substrate. In addition, the thickness of the film could be controlled by using the different amounts of PTFE aqueous emulsion and the relationship between them was shown in Fig. S1 in the Electronic Supplementary Material (ESM). Considering the film quality, 2 mL PTFE aqueous emulsion was used in the fabrication process and the thickness of the corresponding film is about 36 (±2) μm. After that, the composite film was annealed in a CVD at 380 °C for half an hour and the enhanced film could be obtained. As depicted in the SEM image in Fig. 1(e), the shape of PTFE turned from sphere particles to well-connected fusiform-liked particles. The acquired film could be peeled off from the substrate (Fig. 1(f)) and shows the excellent mechanical performance which will be discussed later.

To better understand the obtained MXene material and MXene/PTFE composite film, various characteristic methods were carried to investigate their inner properties. As depicted in Fig. 2(a), it is obvious that the obtained MXene shows an accordion-liked structure, making it have a larger specific area which is helpful for PTFE chain attaching on its surface. Raman spectrum is often investigated to characterize various termination groups and chemical properties of MXene material [56]. As seen in Fig. 2(b), the sharp and intense peak in 153 cm^{-1} indicates the massive production of the relatively large MXene flakes. Next, the distinct sharp peak A1g (Ti, O, C) of MXene appeared around 203 cm^{-1}. Resonance peak of A1g (Ti, Al) appeared around 600 cm^{-1}, however, with the disappearance of Al, peak changes from 610 cm^{-1} (MAX) to 625 cm^{-1} (MXene) and the full width at half-maximum of the peak decreased around 40 cm^{-1}. What's more, a small peak around 509 cm^{-1} indicates the production of small flakes. Additionally, the structural changes of the MAX phase to MXene could also be verified by the XRD patterns in Fig. S2 in the ESM. The disappearance of the characteristic (104) peak located at 39° also indicates the Al atom layer is effectively removed. And the significant shift of (002) peak from 9.5° to 7.8°, which is consistent with previously reported works [57], also illustrating the successful production of $Ti_3C_2T_x$ MXene nanoflakes. What's more, the energy dispersive spectroscopy (EDS) mapping result (Fig. S3 in the ESM) implies a similar conclusion and shows that there are tremendous –F functional groups that are jointed on the surface of MXene.

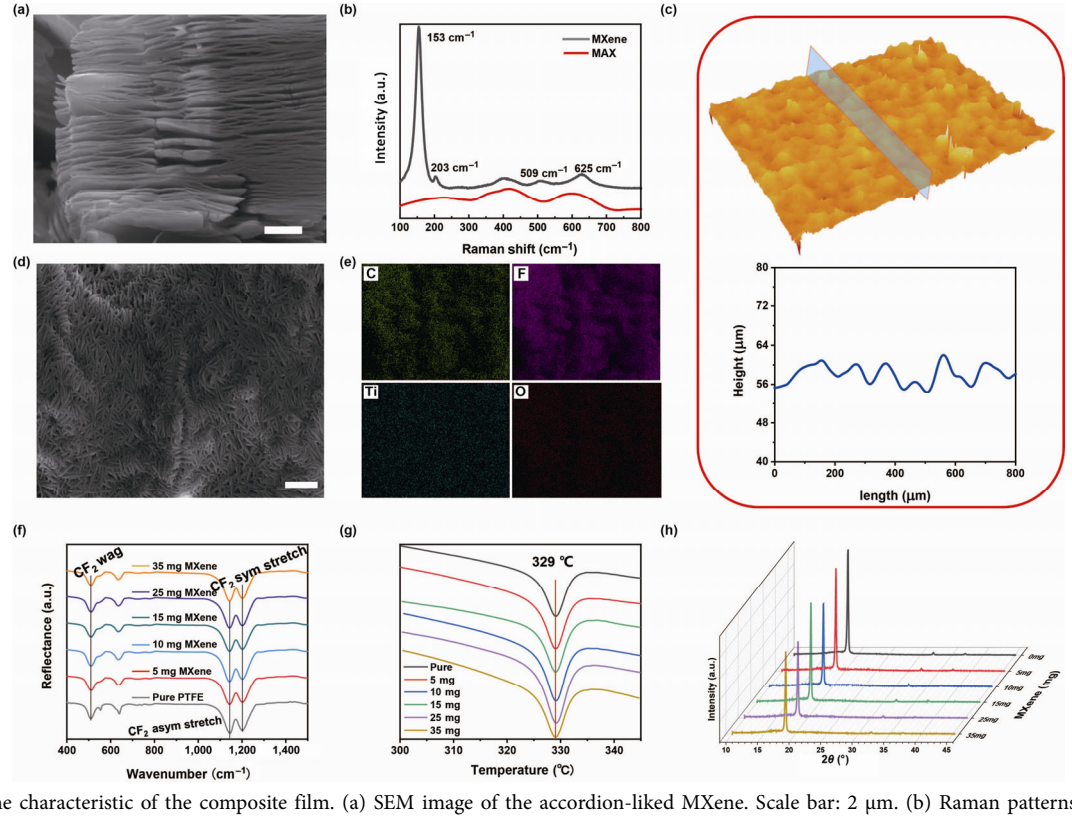

Figure 2 The characteristic of the composite film. (a) SEM image of the accordion-liked MXene. Scale bar: 2 μm. (b) Raman patterns of MAX and MXene. (c) Upper part: three-dimensional image of the MXene/PTFE film with 10 mg MXene doped; Bottom part: crossing section contour of the film. (d) and (e) SEM image and EDS mapping images of the composite film with 10 mg MXene doped. Scale bar: 10 μm. (f) Attenuated total reflectance FTIR patterns of the composite films with doped MXene from 0–35 mg. (g) DSC patterns of composite film with doped MXene from 0–35 mg. (h) XRD patterns of the composite film with doped MXene from 0–35 mg.

It is known that the surface properties of the triboelectric layer have a huge influence on the output performance of the fabricated TENG. By using the confocal microscopy, we find that there is a good deal of micro-humps scattered on the surface of the composite film (Fig. 2(c) upper part) and their scale fluctuating in the vertical direction within 7 μm (Fig. 2(c) bottom part). This is because PTFE nanoparticles are agglomerating in the micro-region during the spraying process and this characteristic contributes to a larger surface area to the obtained MXene/PTFE composite film, which is pretty helpful for increasing its surface charge density. It is known that the color of the MXene flakes is black so that color of the obtained composite film gradually became dark with the increasing amount of MXene, showing that the MXene and PTFE are mixed uniformly (Fig. S4 in the ESM). After that, enlarged images of composite films with the Cu substrate were acquired by an optical microscope (Fig. S5 in the ESM). Because of the agglomerating of nano flakes, it is obvious the size of the MXene flakes inside the film is growing with the increase doping amount of MXene flakes. One more thing worth mentioning that the MXene seen in Fig. S5 in the ESM is just on the focal plane inside the film actually. As for the reason of the reflection of the substrate and optical transparency of the composite film to some extent, it just looks like it's on the surface. Furthermore, EDS was used to investigate the element mapping on the MXene/PTFE composite film (Figs. 2(d) and 2(e)). Consistent with the molecular formulas of MXene and PTFE, the color in C and F are more intensive which indicates that they are the main part of the film. The evenly dispersed Ti also demonstrates the MXene flakes were well mixed with PTFE aqueous, which is important for preparing film with good quality. What's more, the functional groups on the surface of the MXene flakes like –OH or –O, and also may partially oxide MXene to contribute to the existence of O element. For further verification, ATR-FTIR was also carried out, and the result patterns in Fig. 2(f) show that MXene from 0 to 35 mg has little impact on the PTFE phase change. Generally, the CF_2 chain in PTFE is pretty symmetric, and there are no side chains on the main chain, so CF_2 is easy to densely pack and crystallize. Therefore, CF_2 in PTFE film would rearrange to form some special structures which have unique property after annealing process. DSC was used to verify the effect of MXene doping on the crystallinity of the PTFE film. The curve (Fig. 2(g)) shows that the presence of MXene flakes has no effect on the crystal melting point of 329 °C. But the melting enthalpy of the composite film is related to the doping of MXene flakes. For pure PTFE, the melting enthalpy is 24.24 J/g, which is higher than the doped PTFE film (film with 10 mg MXene: 22.61 J/g and film with 35 mg MXene: 20.97 J/g). The corresponding crystallinity of the pure PTFE film, 10 mg doping film and 35 mg doping film is 61%, 56% and 52%, respectively. Meanwhile, the changing crystallinity has a great impact on the mechanical property [58, 59] of the film which will be discussed later. Besides, an evident characteristic peak, which is the main crystallinity peak of PTFE, was observed at 2θ angle of 18.4° in the XRD patterns of all samples. The peak areas of these patterns, which also could be referenced as evidence to represent the crystallinity of the composite films [60], indicate a similar result with the DSC analysis.

To investigate the effect of MXene sheet in PTFE film on the mechanical properties of composite membrane, the shape of MXene/PTFE composite membrane was customized to a standard rectangle (Fig. 3(a)), and then stretched by a universal testing machine to breakage. As depicted in Fig. 3(b), it is evident that all the MXene doped composite films show better mechanical property than the pure PTFE film. Particularly, the composite film with 10 mg MXene demonstrates the best

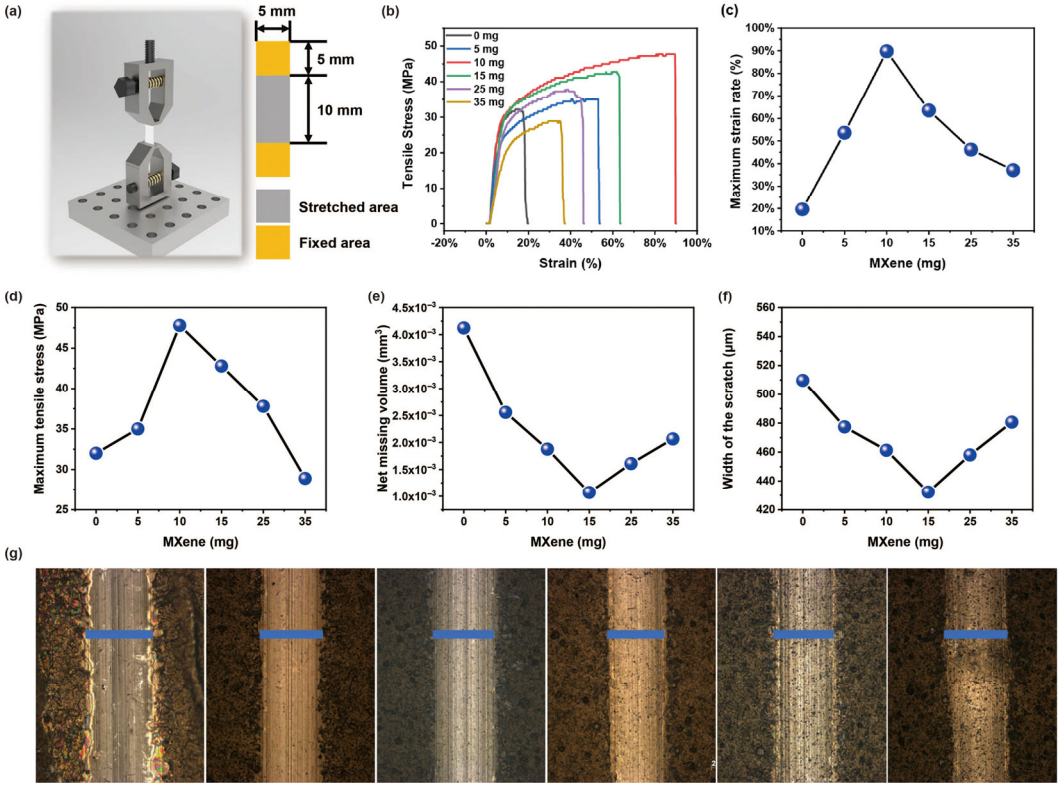

Figure 3 The mechanical property of the MXene enhanced film. (a) Illustration of the stretch condition in the tensile test. (b) The stress and strain relationships of the composite films with doped MXene from 0–35 mg in tensile test. (c) The maximum stress and the (d) maximum strain rate of the composite film with doped MXene from 0–35 mg in tensile test. (e) The net missing volume and (f) the width of the scratch of the composite films with doped MXene from 0–35 mg in friction test. (g) Photographs of the composite film with doped MXene from 0–35 mg (from left to right) rubbed for 1 h under 1 N pressure.

performance. In detail, the maximum strain rate of all composite films has improved to some extent than the pure PTFE film, and the composite film with 10 mg MXene reaches the highest, which is as large as 90 % and it is 450% more than that of the pure PTFE film (strain rate is 20 %). As the doping amount of MXene flakes increasing further (more than 10 mg), this property of the composite film begins to drop off (Fig. 3(c)). Coincidently, the maximum tensile stress illustrates the same trend as the maximum strain rate. The composite film with 10 mg MXene shows the maximal tensile stress of 48 MPa, which is also 50% larger than that of pure PTFE film (32 MPa). What's more, with the amount of MXene flakes increase to 35 mg, the tensile stress of the composite film becomes lower than that of the virginal PTFE film (Fig. 3(d)). As seen in Fig. S6 in the ESM, the mechanism of the mechanical enhancement effect is attributed to the addition of the MXene flakes. It is known that the MXene is a new kind of two-dimensional ceramic material and its surface has a lot of functional groups such as –F, which has been verified before. At the same time, $-CF_2$, which is a carbon atom connected with two fluorine atoms, is the basic unit of the PTFE film. Based on the analysis, one of the possible enhancement effects is related to the intermolecular force. At the interface between MXene sheet and CF_2 chain, the fluorine atoms are in the overlapping force field area caused by the titanium atoms and the carbon atoms, so that the fluorine atoms act as a bridge that firmly binds the two materials together. In addition, the surface of MXene flakes is rough, which can provide many salient points for the CF_2 chain attach, resulting in a good adhesion between the CF_2 chain and the MXene flakes. Therefore, when the composite membrane is stretched under the action of external force, inside the PTFE membrane, numerous MXene flakes hinder the dislocation movement of the CF_2 chain which often result in cracks, and form many strength enhanced areas which is similar to the reinforced concrete structure. Thus, as seen in Fig. S6(a) in the ESM, plenty of reinforced areas are constructed to make the composite film have better mechanical properties. However, with the further increase of MXene doping, MXene flakes tend to agglomerate together, which is due to the weak van der Waals force. These agglomerated grains are the potential split areas that are easily propagated to cracks under external force, resulting in the break of the film. And this has been observed on the SEM images (Fig. S7 in the ESM) of the composite film with doped MXene of 0, 10, and 35 mg. It is obvious that the increase of MXene will lead to the production of some little cracks on the surface of the composite film. The crystallinity of the PTFE is another critical reason related to its mechanical enhancement. It is known that the crystalline region in PTFE film has good strength and hardness but has poor deformability, while the amorphous area has an opposite property. As illustrated in Fig. S6(b) in the ESM, without heterogeneous material, there are many crystalline bulks formed during the annealing stage and this process would cause a local and limited amorphous region distribution inside the film. This kind of structure will make the film have poor deformability. However, the doping MXene will break the bulk crystalline region into many small pieces and decrease the crystallinity of the film (from 61% to 52%) which has been verified in the DSC testing. Hence, the evenly distributed amorphous area makes the film have better stretchability.

Step further, friction test was also carried to check the wear resistance property of the composite film. As seen in Fig. S8 in the ESM, a steel grinding ball is applied to rub the surface of composite films back and forth with a vertical force of 1 N for 3,600 s. As shown in Fig. 3(e), the missing volume of rubbed film has been calculated and the composite film with 15 mg MXene doping shows the least miss part of 1.07×10^{-3} mm^3. On the contrary, the pure PTFE film loses 4.12×10^{-3} mm^3, which is almost 4 times larger. However, as the doping amount of MXene starts from 15 mg, the missing part further increases because the debris are more easily to be generated by defects that are more likely to appear on the surface of the heavily doped composite film. Coincidently, a similar trend shows on the width of the rubbed trace of each film (Figs. 3(f) and 3(g)). What's more, vertical load from 0.2 to 4 N acted on the surface of the films and rubbed for 30 s in every test. As shown in Fig. S9 in the ESM, under the weak force, wear scar width of the film is decreasing as the doped MXene increasing. As the force is increased to 3 N, the pure PTFE film wears first, and the composite film doped with 5 mg MXene also shows signs of cracking (red circled area). Oppositely, other composite films are quite stable. But all the film can't bear the friction and torn by the steel grinding ball at 4 N. This result also shows the strength enhancement effect of the doping MXene.

Furthermore, the electrical performance of fabricated TENG with size of 5 cm × 5 cm × 0.5 cm was tested in contact-separation mode by a commercial linear motor as seen in Fig. S10 in the ESM. The typical four working steps of this kind of TENG are shown in Fig. 4(a). At the initial stage, the two triboelectric layers with opposite electronegative property contact with each other and the electron will transfer from the volatile electron layer (Cu) to the electronegative layer (PTFE). Because of the electric field shielding, there is no electron movement in the external circuit at this moment. At stage ii, Cu layer begins to separate from the interface and electrons are kept on the surface of PTFE film which causes an unbalanced electric field on the PTFE surface. To keep the electric field back into equilibrium, some charges driven by induced electric field are flowing from bottom electrode to ground. At stage iii, Cu layer moving to the farthermost position, charges induced on the bottom reach the maximum and electrons keep flowing to the ground on external circuit in this process. At stage iv, as the top Cu layer getting close to the PTFE layer, the equilibrium electric field is broken again and electrons flow back to the bottom Cu electrode through the external circuit. As the top Cu layer contact with the PTFE layer, this system goes back into the initial condition and is ready for next circle. During these processes, electron flows back and forth in the external circuit driving the load to work. To have a better understanding of the enhancement effect of the MXene/PTFE based TENG, capacitor models are established in Fig. S11 in the ESM. As shown in Fig. S11(a) in the ESM, the typical capacitor model can be described like this [61]

$$C = (\varepsilon_0 \cdot \varepsilon_r \cdot S)/d \quad (1)$$

Where ε_0, ε_r, S and d represent vacuum permittivity, relative permittivity, surface area of the electrode, and the thickness of the dielectric layer. Based on this model, when the electrodes with the thickness of r were inserted into the dielectric layer, the total capacitance became larger as it is contributed by four series capacitors, as shown in Fig. S11(b) in the ESM, and the capacitance can be described below

$$C = (\varepsilon_0 \cdot \varepsilon_r \cdot S)/(d-3r) \quad (2)$$

Thus, if i pieces of electrodes inserted, the equivalent capacitance should be

$$C = (\varepsilon_0 \cdot \varepsilon_r \cdot S)/(d-ir) \quad (3)$$

We can learn from the equation that the capacitance rises as the number of the electrode inside the dielectric increases. The real and simplified distribution models of the MXene flakes are

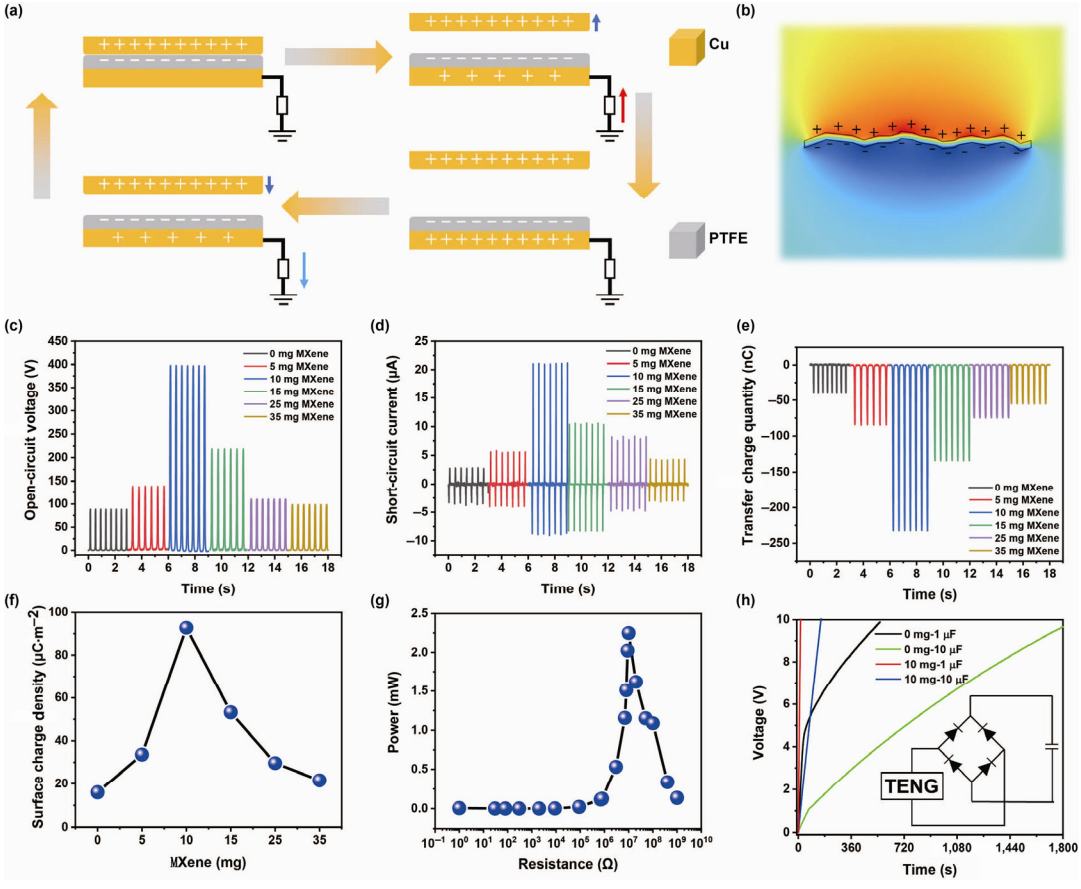

Figure 4 Electric output performance of the fabricated TENG. (a) Working mechanism of the as fabricated TENG. (b) Finite element analysis of the charge distribution on a MXene flake. (c)–(f) The open-circuit voltage, the shot-circuit current and the surface charge density of the TENG fabricated by composite film with doped MXene from 0–35 mg. (g) the output power of the TENG with external resistance. (h) Using the Pure-PTFE film and 10 mg MXene doped composite film fabricated TENG charge for capacitors with the capacity of 1 μF and 10 μF, respectively.

shown in Figs. S11(c) and S11(d) in the ESM. k represents the number of MXene flakes in the vertical direction and i represents the number of MXene flakes in the horizontal direction. Thus, the equivalent capacitance can be calculated as follow

$$C = (\varepsilon_0 \cdot \varepsilon_r \cdot S)/d + \varepsilon_0 \cdot \varepsilon_r \cdot k \cdot a(1/(d - ir) - 1/d) \quad (4)$$

where a represents the area of a single MXene flake. Consequently, numerous micro-capacitors created by filling the MXene flakes in the PTFE film have a great enhancement effect on the capacity of the capacitor, thereby improving the energy storage in the capacitor and promoting the performance of the fabricated TENG. As mentioned before, MXene flakes have a rough surface resulting in a higher specific area, as shown in the corresponding finite element analysis (FEA) simulation model in Fig. 4(b). When a high voltage is applied, a larger specific surface provides more area for charge to accumulate, resulting in more positive charges induced on the upper interface of MXene flake and PTFE. Meanwhile, more negative charges induced on the bottom interface between the two. Therefore, countless charged interface in the film contributes to a higher voltage in the whole structure and leading to a better electrical performance.

To validate the theory, electrical output of the fabricated TENG with MXene from 0 to 35 mg is investigated. Figure 4(c) shows the open-circuit voltage of the TENG and output voltage increase with the increasing fraction of MXene from 0 to 10 mg and reach a peak voltage of almost 400 V. Then with MXene increasing further, output voltage decreases and shows the same performance with pure PTFE film as MXene at 35 mg. And short-circuit current in Fig. 4(d) shows a similar trend with the voltage output (Fig. S12 in the ESM). And the TENG with 10 mg MXene shows the best current output of 21 μA, which is almost 6 times higher than that of pure PTFE film. The transfer charge quantity of the TENG with 10 mg MXene also shows a peak performance of 232 nC (the corresponding surface charge density is 92.8 μC/m^2) which is 6 times higher than that of pure PTFE film too (Figs. 4(e) and 4(f)). The output voltage and current of the TENG with 10 mg MXene are also measured under different resistance from 0 to 1 GΩ. As presented in Fig. S13 in the ESM, it can be told that the voltage and current keep stable when the external load under 1 MΩ. And between 1 and 100 MΩ, both the voltage and current varied sharply and gradually back to stable state after the load more than 100 MΩ. In addition, the output power could be calculated ($P = U^2/R$) and the maximum power of 2.25 mW reached as the external load at 10 MΩ (Fig. 4(g)). To contrast the output performance of TENG fabricated by composite film of 10 mg MXene and pure PTFE film, TENG were connected with a rectifier bridge and charge for capacitors, as shown in Fig. 4(h). Time for charging the capacitors of 1, 10 μF to 10 V by TENG with 10 mg MXene are just 15 and 154 s respectively. On the contrary, TENG fabricated by pure PTFE film charging for the same capacitors are spending at least 550 and 1,786 s which is more than 37 and 11 times slower than that of the composite film. This result clearly shows that electrical performance of the TENG could be greatly enhanced by the doping of MXene flakes into the PTFE film. Finally, 100,000 cycles test was carried on to verify the durability of the fabricated TENG. As illustrated in Fig. S14, there is no significant attenuation during the test. And the SEM images displayed in Fig. S15 in the

ESM demonstrate the surface morphologies of the composite film with 10 mg MXene before (Fig. S15(a) in the ESM) and after (Fig. S15(b) in the ESM) the 100000 cycles test and there has no distinct variance which shows the excellent stability of the MXene/PTFE based TENG.

4 Conclusion

In summary, we fabricate a MXene based mechanically and electrically enhanced PTFE composite film for TENG. Different amount of MXene was doped into PTFE and corresponding performance was investigated systematically. We find that the addition of MXene could affect the crystallinity of the PTFE film as well as energy storage of the composite film which have a great impact on the mechanical performance and TENG output of the fabricated device. Finally, the composite film with 10 mg MXene shows the best strain rate of 90% and tensile strength of 48 MPa, which is 450% and 50% larger than that of the pure PTFE film. As the MXene increases to 15 mg, the wear resistance evidently improved and the 80% wear volume of the film during the friction test is reduced than the pure PTFE film. These properties make the film could keep stable in various complicate environments. Coincidently, because of the numerous micro-capacitors formed inside the PTFE film by MXene, TENG with 10 mg MXene also shows the best electrical performance, open-circuit voltage of 397 V, short-circuit current of 21 μA and transfer charge quantity of 232 nC which is 4, 6, 6 times higher than that of pure PTFE film. Therefore, the TENG made by the MXene/PTFE composite film has good mechanical and electrical performance at the same time which makes it a good candidate for some complicated environments.

Acknowledgements

The authors thank the support of the National Natural Science Foundation of China (Nos. 51922023 and 61874011), National Key Research and Development Program of China (No. 2016YFA0202704), Beijing Talents Foundation (No. 2017000021223TD04), Tribology Science Fund of State Key Laboratory of Tribology (No. SKLTKF19B02), Open Research Foundation of State Key Laboratory of Digital Manufacturing Equipment & Technology (DMETKF2020014), and Young Scientific and Technological Innovation Research Team Funds of Sichuan Province (No. 20CXTD0106). Furthermore, the authors are grateful to Dr. Weijie Sun, who work as an engineer of material analysis test center of Beijing Institute of Nanoenergy and Nanosystems, for the material characterization.

Electronic Supplementary Material: Supplementary material (further detailed characterizations of the composite film, illustration of the mechanical enhancement mechanism, testing method, images of rubbed composite film, durability test of the composite film) is available in the online version of this article at https://doi.org/10.1007/s12274-021-3437-5.

References

[1] Yu, X.; Xie, Z. Q.; Yu, Y.; Lee, J.; Vazquez-Guardado, A.; Luan, H. W.; Ruban, J.; Ning, X.; Akhtar, A.; Li, D. F. et al. Skin-integrated wireless haptic interfaces for virtual and augmented reality. *Nature* **2019**, *575*, 473–479.

[2] Zhou, Z. H.; Chen, K.; Li, X. S.; Zhang, S. L.; Wu, Y. F.; Zhou, Y. H.; Meng, K. Y.; Sun, C. C.; He, Q.; Fan, W. J. et al. Sign-to-speech translation using machine-learning-assisted stretchable sensor arrays. *Nat. Electron.* **2020**, *3*, 571–578.

[3] Meng, K. Y.; Zhao, S. L.; Zhou, Y. H.; Wu, Y. F.; Zhang, S. L.; He, Q.; Wang, X.; Zhou, Z. H.; Fan, W. J.; Tan, X. L. et al. A wireless textile-based sensor system for self-powered personalized health care. *Matter* **2020**, *2*, 896–907.

[4] Yan, C.; Gao, Y. Y.; Zhao, S. L.; Zhang, S. L.; Zhou, Y. H.; Deng, W. L.; Li, Z. W.; Jiang, G.; Jin, L.; Tian, G. et al. A linear-to-rotary hybrid nanogenerator for high-performance wearable biomechanical energy harvesting. *Nano Energy* **2019**, *67*, 104235.

[5] Lin, Z. M.; Yang, J.; Li, X. S.; Wu, Y. F.; Wei, W.; Liu, J.; Chen, J.; Yang, J. Large-scale and washable smart textiles based on triboelectric nanogenerator arrays for self-powered sleeping monitoring. *Adv. Funct. Mater.* **2018**, *28*, 1704112.

[6] Meng, K. Y.; Chen, J.; Li, X. S.; Wu, Y. F.; Fan, W. J.; Zhou, Z. H.; He, Q.; Wang, X.; Fan, X.; Zhang, Y. X. et al. Flexible weaving constructed self-powered pressure sensor enabling continuous diagnosis of cardiovascular disease and measurement of cuffless blood pressure. *Adv. Funct. Mater.* **2019**, *29*, 1806388.

[7] Tian, G.; Deng, W. L.; Gao, Y. Y.; Xiong, D.; Yan, C.; He, X. B.; Yang, T.; Jin, L.; Chu, X.; Zhang, H. T. et al. Rich lamellar crystal baklava-structured PZT/PVDF piezoelectric sensor toward individual table tennis training. *Nano Energy* **2019**, *59*, 574–581.

[8] Tat, T.; Libanori, A.; Au, C.; Yau, A.; Chen, J. Advances in triboelectric nanogenerators for biomedical sensing. *Biosens. Bioelectron.* **2020**, *171*, 112714.

[9] Zhang, B. B.; Zhang, L.; Deng, W. L.; Jin, L.; Chun, F. J.; Pan, H.; Gu, B. N.; Zhang, H. T.; Lv, Z. K.; Yang, W. Q. et al. Self-powered acceleration sensor based on liquid metal triboelectric nanogenerator for vibration monitoring. *ACS Nano* **2017**, *11*, 7440–7446.

[10] Chen, G. R.; Li, Y. Z.; Bick, M.; Chen, J. Smart textiles for electricity generation. *Chem. Rev.* **2020**, *120*, 3668–3720.

[11] Zhang, N. N.; Huang, F.; Zhao, S. L.; Lv, X. H.; Zhou, Y. H.; Xiang, S. W.; Xu, S. M.; Li, Y. Z.; Chen, G. R.; Tao, C. Y. et al. Photo-rechargeable fabrics as sustainable and robust power sources for wearable bioelectronics. *Matter* **2020**, *2*, 1260–1269.

[12] Chen, J.; Huang, Y.; Zhang, N. N.; Zou, H. Y.; Liu, R. Y.; Tao, C. Y.; Fan, X.; Wang, Z. L. Micro-cable structured textile for simultaneously harvesting solar and mechanical energy. *Nat. Energy* **2016**, *1*, 16138.

[13] Zhang, N. N.; Chen, J.; Huang, Y.; Guo, W. W.; Yang, J.; Du, J.; Fan, X.; Tao, C. Y. A wearable all-solid photovoltaic textile. *Adv. Mater.* **2016**, *28*, 263–269.

[14] Zou, Y. J.; Libanori, A.; Xu, J.; Nashalian, A.; Chen, J. Triboelectric nanogenerator enabled smart shoes for wearable electricity generation. *Research* **2020**, *2020*, 7158953.

[15] Zhu, G.; Zhou, Y. S.; Bai, P.; Meng, X. S.; Jing, Q. S.; Chen, J.; Wang, Z. L. A shape-adaptive thin-film-based approach for 50% high-efficiency energy generation through micro-grating sliding electrification. *Adv. Mater.* **2014**, *26*, 3788–3796.

[16] Gao, L. X.; Chen, X.; Lu, S.; Zhou, H.; Xie, W. B.; Chen, J. F.; Qi, M. K.; Yu, H.; Mu, X. J.; Wang, Z. L.; Yang, Y. Enhancing the output performance of triboelectric nanogenerator via grating-electrode-enabled surface plasmon excitation. *Adv. Energy Mater.* **2019**, *9*, 1902725.

[17] Chen, J.; Guo, H. Y.; Wu, Z. Y.; Xu, G. Q.; Zi, Y. L.; Hu, C. G.; Wang, Z. L. Actuation and sensor integrated self-powered cantilever system based on TENG technology. *Nano Energy* **2019**, *64*, 103920.

[18] Guo, H.; Zhao, J. Q.; Dong, Q. S.; Wang, L. D.; Ren, X. Y.; Liu, S.; Zhang, C.; Dong, G. F. A self-powered and high-voltage-isolated organic optical communication system based on triboelectric nanogenerators and solar cells. *Nano Energy* **2019**, *56*, 391–399.

[19] Liang, X.; Jiang, T.; Liu, G. X.; Feng, Y. W.; Zhang, C.; Wang, Z. L. Spherical triboelectric nanogenerator integrated with power management module for harvesting multidirectional water wave energy. *Energ Environ. Sci.* **2020**, *13*, 277–285.

[20] Wang, Z. L.; Wang, A. C. On the origin of contact-electrification. *Mater. Today* **2019**, *30*, 34–51.

[21] Wang, Z. L. On the first principle theory of nanogenerators from Maxwell's equations. *Nano Energy* **2019**, *68*, 104272.

[22] Jie, Y.; Ma, J. M.; Chen, Y. D.; Cao, X.; Wang, N.; Wang, Z. L. Efficient delivery of power generated by a rotating triboelectric nanogenerator by conjunction of wired and wireless transmissions using Maxwell's displacement currents. *Adv. Energy Mater.* **2018**, *8*, 1802084.

[23] Deng, W. L.; Zhou, Y. H.; Zhao, X.; Zhang, S. L.; Zou, Y. J.; Xu, J.; Yeh, M. H.; Guo, H. Y.; Chen, J. Ternary electrification layered

architecture for high-performance triboelectric nanogenerators. *ACS Nano* **2020**, *14*, 9050–9058.

[24] Wang, H. M.; Li, D.; Zhong, W.; Xu, L.; Jiang, T.; Wang, Z. L. Self-powered inhomogeneous strain sensor enabled joint motion and three-dimensional muscle sensing. *ACS Appl. Mater. Interfaces* **2019**, *11*, 34251–34257.

[25] Tan, P. C.; Zheng, Q.; Zou, Y.; Shi, B. J.; Jiang, D. J.; Qu, X. C.; Ouyang, H.; Zhao, C. C.; Cao, Y.; Fan, Y. B. et al. A battery-like self-charge universal module for motional energy harvest. *Adv. Energy Mater.* **2019**, *9*, 1901875.

[26] Liang, X.; Jiang, T.; Feng, Y. W.; Lu, P. J.; An, J.; Wang, Z. L. Triboelectric nanogenerator network integrated with charge excitation circuit for effective water wave energy harvesting. *Adv. Energy Mater.* **2020**, *10*, 2002123.

[27] Ren, Z. W.; Wang, Z. M.; Liu, Z. R.; Wang, L. F.; Guo, H. Y.; Li, L. L.; Li, S. T.; Chen, X. Y.; Tang, W.; Wang, Z. L. Energy harvesting from breeze wind (0.7–6 $m \cdot s^{-1}$) using ultra-stretchable triboelectric nanogenerator. *Adv. Energy Mater.* **2020**, *10*, 2001770.

[28] Zhou, Y. H.; Deng, W. L.; Xu, J.; Chen, J. Engineering materials at the nanoscale for triboelectric nanogenerators. *Cell Rep. Phys. Sci.* **2020**, *1*, 100142.

[29] Xu, J.; Zou, Y. J.; Nashalian, A.; Chen, J. Leverage surface chemistry for high-performance triboelectric nanogenerators. *Front. Chem.* **2020**, *8*, 577327.

[30] Chen, J.; Wang, Z. L. Reviving vibration energy harvesting and self-powered sensing by a triboelectric nanogenerator. *Joule* **2017**, *1*, 480–521.

[31] Jing, Q. S.; Zhu, G.; Bai, P.; Xie, Y. N.; Chen, J.; Han, R. P. S.; Wang, Z. L. Case-encapsulated triboelectric nanogenerator for harvesting energy from reciprocating sliding motion. *ACS Nano* **2014**, *8*, 3836–3842.

[32] Chen, J.; Yang, J.; Guo, H. Y.; Li, Z. L.; Zheng, L.; Su, Y. J.; Wen, Z.; Fan, X.; Wang, Z. L. Automatic mode transition enabled robust triboelectric nanogenerators. *ACS Nano* **2015**, *9*, 12334–12343.

[33] Wang, S. L.; Lin, L.; Wang, Z. L. Triboelectric nanogenerators as self-powered active sensors. *Nano Energy* **2015**, *11*, 436–462.

[34] Lin, Z. M.; Chen, J.; Li, X. S.; Zhou, Z. H.; Meng, K. Y.; Wei, W.; Yang, J.; Wang, Z. L. Triboelectric nanogenerator enabled body sensor network for self-powered human heart-rate monitoring. *ACS Nano* **2017**, *11*, 8830–8837.

[35] Bai, P.; Zhu, G.; Jing, Q. S.; Yang, J.; Chen, J.; Su, Y. J.; Ma, J. S.; Zhang, G.; Wang, Z. L. Membrane-based self-powered triboelectric sensors for pressure change detection and its uses in security surveillance and healthcare monitoring. *Adv. Funct. Mater.* **2014**, *24*, 5807–5813.

[36] Zhou, Z. H.; Padgett, S.; Cai, Z. X.; Conta, G.; Wu, Y. F.; He, Q.; Zhang, S. L.; Sun, C. C.; Liu, J.; Fan, E. D. et al. Single-layered ultra-soft washable smart textiles for all-around ballistocardiograph, respiration, and posture monitoring during sleep. *Biosens. Bioelectron.* **2020**, *155*, 112064.

[37] Su, Y. J.; Yang, T. N.; Zhao, X.; Cai, Z. X.; Chen, G. R.; Yao, M. L.; Chen, K.; Bick, M.; Wang, J. J.; Li, S. D. et al. A wireless energy transmission enabled wearable active acetone biosensor for non-invasive prediabetes diagnosis. *Nano Energy* **2020**, *74*, 104941.

[38] Yang, J.; Chen, J.; Su, Y. J.; Jing, Q. S.; Li, Z. L.; Yi, F.; Wen, X. N.; Wang, Z. N.; Wang, Z. L. Eardrum-inspired active sensors for self-powered cardiovascular system characterization and throat-attached anti-interference voice recognition. *Adv. Mater.* **2015**, *27*, 1316–1326.

[39] Wu, Y.; Jing, Q. S.; Chen, J.; Bai, P.; Bai, J. J.; Zhu, G.; Su, Y. J.; Wang, Z. L. A self-powered angle measurement sensor based on triboelectric nanogenerator. *Adv. Funct. Mater.* **2015**, *25*, 2166–2174.

[40] Zou, H. Y.; Zhang, Y.; Guo, L. T.; Wang, P. H.; He, X.; Dai, G. Z.; Zheng, H. W.; Chen, C. Y.; Wang, A. C.; Wang, Z. L. et al. Quantifying the triboelectric series. *Nat. Commun.* **2019**, *10*, 1427.

[41] Dudem, B.; Kim, D. H.; Mule, A. R.; Yu, J. S. Enhanced performance of microarchitectured PTFE-based triboelectric nanogenerator via simple thermal imprinting lithography for self-powered electronics. *ACS Appl. Mater. Interfaces* **2018**, *10*, 24181–24192.

[42] Chun, S.; Choi, I. Y.; Son, W.; Jung, J.; Lee, S.; Kim, H. S.; Pang, C.; Park, W.; Kim, J. K. High-output and bending-tolerant triboelectric nanogenerator based on an interlocked array of surface-functionalized indium tin oxide nanohelixes. *ACS Energy Letters* **2019**, *4*, 1748–1754.

[43] Wang, S. H.; Xie, Y. N.; Niu, S. M.; Lin, L.; Liu, C.; Zhou, Y. S.; Wang, Z. L. Maximum surface charge density for triboelectric nanogenerators achieved by ionized-air injection: Methodology and theoretical understanding. *Adv. Mater.* **2014**, *26*, 6720–6728.

[44] Chen, J.; Guo, H.; He, X. M.; Liu, G. L.; Xi, Y.; Shi, H. F.; Hu, C. G. Enhancing performance of triboelectric nanogenerator by filling high dielectric nanoparticles into sponge PDMS film. *ACS Appl. Mater. Interfaces* **2016**, *8*, 736–744.

[45] Paria, S.; Si, S. K.; Karan, S. K.; Das, A. K.; Maitra, A.; Bera, R.; Halder, L.; Bera, A.; De, A.; Khatua, B. B. A strategy to develop highly efficient TENGs through the dielectric constant, internal resistance optimization, and surface modification. *J. Mater. Chem. A* **2019**, *7*, 3979–3991.

[46] Zhu, G.; Lin, Z. H.; Jing, Q. S.; Bai, P.; Pan, C. F.; Yang, Y.; Zhou, Y. S.; Wang, Z. L. Toward large-scale energy harvesting by a nanoparticle-enhanced triboelectric nanogenerator. *Nano Lett.* **2013**, *13*, 847–853.

[47] Chen, B. D.; Tang, W.; Zhang, C.; Xu, L.; Zhu, L. P.; Yang, L. J.; He, C.; Chen, J.; Liu, L.; Zhou, T. et al. Au nanocomposite enhanced electret film for triboelectric nanogenerator. *Nano Res.* **2018**, *11*, 3096–3105.

[48] Jin, L.; Xiao, X.; Deng, W. L.; Nashalian, A.; He, D. R.; Raveendran, V.; Yan, C.; Su, H.; Chu, X.; Yang, T. et al. Manipulating relative permittivity for high-performance wearable triboelectric nanogenerators. *Nano Lett.* **2020**, *20*, 6404–6411.

[49] Naguib, M.; Kurtoglu, M.; Presser, V.; Lu, J.; Niu, J. J.; Heon, M.; Hultman, L.; Gogotsi, Y.; Barsoum, M. W. Two-dimensional nanocrystals produced by exfoliation of Ti_3AlC_2. *Adv. Mater.* **2011**, *23*, 4248–4253.

[50] Cheng, Y.; Ma, Y. N.; Li, L. Y.; Zhu, M.; Yue, Y.; Liu, W. J.; Wang, L. F.; Jia, S. F.; Li, C.; Qi, T. Y. et al. Bioinspired microspines for a high-performance spray $Ti_3C_2T_x$ MXene-based piezoresistive sensor. *ACS Nano* **2020**, *14*, 2145–2155.

[51] Gao, Y. Y.; Yan, C.; Huang, H. C.; Yang, T.; Tian, G.; Xiong, D.; Chen, N. J.; Chu, X.; Zhong, S.; Deng, W. L. et al. Microchannel-confined MXene based flexible piezoresistive multifunctional micro-force sensor. *Adv. Funct. Mater.* **2020**, *30*, 1909603.

[52] Xu, H.; Ren, A. B.; Wu, J.; Wang, Z. M. Recent advances in 2D MXenes for photodetection. *Adv. Funct. Mater.* **2020**, *30*, 2000907.

[53] Abdolhosseinzadeh, S.; Schneider, R.; Verma, A.; Heier, J.; Nüesch, F.; Zhang, C. F. Turning trash into treasure: Additive free MXene sediment inks for screen-printed micro-supercapacitors. *Adv. Mater.* **2020**, *32*, 2000716.

[54] Anasori, B.; Lukatskaya, M. R.; Gogotsi, Y. 2D metal carbides and nitrides (MXenes) for energy storage. *Nat. Rev. Mater.* **2017**, *2*, 16098.

[55] Dong, Y. C.; Mallineni, S. S. K.; Maleski, K.; Behlow, H.; Mochalin, V. N.; Rao, A. M.; Gogotsi, Y.; Podila, R. Metallic MXenes: A new family of materials for flexible triboelectric nanogenerators. *Nano Energy* **2018**, *44*, 103–110.

[56] Sarycheva, A.; Gogotsi, Y. Raman spectroscopy analysis of the structure and surface chemistry of $Ti_3C_2T_x$ MXene. *Chem. Mater.* **2020**, *32*, 3480–3488.

[57] Ma, Y. N.; Liu, N. S.; Li, L. Y.; Hu, X. K.; Zou, Z. G.; Wang, J. B.; Luo, S. J.; Gao, Y. H. A highly flexible and sensitive piezoresistive sensor based on MXene with greatly changed interlayer distances. *Nat. Commun.* **2017**, *8*, 1207.

[58] Sciuti, V. F.; Melo, C. C.; Canto, L. B.; Canto, R. B. Influence of surface crystalline structures on DSC analysis of PTFE. *Mater. Res.* **2017**, *20*, 1350–1359.

[59] Conte, M.; Pinedo, B.; Igartua, A. Role of crystallinity on wear behavior of PTFE composites. *Wear* **2013**, *307*, 81–86.

[60] Lebedev, Y. A.; Korolev, Y. M.; Polikarpov, V. M.; Ignat'eva, L. N.; Antipov, E. M. X-ray powder diffraction study of polytetrafluoroethylene. *Crystallogr. Rep.* **2010**, *55*, 609–614.

[61] Xia, X. N.; Chen, J.; Guo, H. Y.; Liu, G. L.; Wei, D. P.; Xi, Y.; Wang, X.; Hu, C. G. Embedding variable micro-capacitors in polydimethylsiloxane for enhancing output power of triboelectric nanogenerator. *Nano Res.* **2016**, *10*, 320–330.